Switching characteristics of an InP photonic crystal nanocavity: Experiment and theory

Yu, Yi; Palushani, Evarist; Heuck, Mikkel; Kuznetsova, Nadezda; Kristensen, Philip Trøst; Ek, Sara; Vukovic, Dragana; Peucheret, Christophe; Oxenløwe, Leif Katsuo; Combrié, Sylvain

Total number of authors:
13

Published in:
Optics Express

Link to article, DOI:
10.1364/OE.21.031047

Publication date:
2013

Document Version
Publisher's PDF, also known as Version of record

Switching characteristics of an InP photonic crystal nanocavity: Experiment and theory

Yi Yu,[1,*] Evarist Palushani,[1] Mikkel Heuck,[1] Nadezda Kuznetsova,[1] Philip Trøst Kristensen,[1] Sara Ek,[1] Dragana Vukovic,[1] Christophe Peucheret,[1] Leif Katsuo Oxenløwe,[1] Sylvain Combrié,[2] Alfredo de Rossi,[2] Kresten Yvind,[1] and Jesper Mørk[1]

[1]DTU Fotonik, Technical University of Denmark, DK-2800 Kongens Lyngby, Denmark
[2]Thales Research and Technology, France, Avenue A. Fresnel, 91767 Palaiseau, France
[*]yiyu@fotonik.dtu.dk

Abstract: The dynamical properties of an InP photonic crystal nanocavity are experimentally investigated using pump-probe techniques and compared to simulations based on coupled-mode theory. Excellent agreement between experimental results and simulations is obtained when employing a rate equation model containing three time constants, that we interpret as the effects of fast carrier diffusion from an initially localized carrier distribution and the slower effects of surface recombination and bulk recombination. The variation of the time constants with parameters characterizing the nanocavity structure is investigated. The model is further extended to evaluate the importance of the fast and slow carrier relaxation processes in relation to patterning effects in the device, as exemplified by the case of all-optical wavelength conversion.

OCIS codes: (190.4360) Nonlinear optics, devices; (050.5298) Photonic crystals; (200.6715) Switching; (130.3120) Integrated optics devices.

References and links

1. D. A. B. Miller, "Device requirements for optical interconnects to silicon chips," Proc. IEEE **97**(7), 1166 (2009).
2. M. Notomi, A. Shinya, K. Nozaki, T. Tanabe, S. Matsuo, E. Kuramochi, T. Sato, H. Taniyama, and H. Sumikura, "Low-power nanophotonic devices based on photonic crystals towards dense photonic network on chip," IET Circuits Devices Syst. **5**(2), 84–93 (2011).
3. O. Wada, "Recent progress in semiconductor-based photonic signal-processing devices," IEEE J. Sel. Top. Quantum Electron. **17**(2), 309–319 (2011).
4. P. A. Andrekson, H. Sunnerud, S. Oda, T. Nishitani, and J. Yang, "Ultrafast, atto-Joule switch using fiber-optic parametric amplifier operated in saturation," Opt. Express **16**(15), 10956–10961 (2008).
5. M. Waldow, T. Plötzing, M. Gottheil, M. Först, J. Bolten, T. Wahlbrink, and H. Kurz, "25ps all-optical switching in oxygen implanted silicon-on-insulator microring resonator," Opt. Express **16**(11), 7693–7702 (2008).
6. L. O'Faolain, D. M. Beggs, T. P. White, T. Kampfrath, K. Kuipers, and T. F. Krauss, "Compact optical switches and modulators based on dispersion engineered photonic crystals," IEEE Photonics J. **2**(3), 404–414 (2010).
7. C. Koos, P. Vorreau, T. Vallaitis, P. Dumon, W. Bogaerts, R. Baets, B. Esembeson, I. Biaggio, T. Michinobu, F. Diederich, W. Freude, and J. Leuthold, "All-optical high-speed signal processing with silicon-organic hybrid slot waveguides," Nat. Photonics **4**, 216–219 (2010).
8. T. Tanabe, K. Nishiguchi, A. Shinya, E. Kuramochi, H. Inokawa, M. Notomi, K. Yamada, T. Tsuchizawa, T. Watanabe, H. Fukuda, H. Shinojima, and S. Itabashi, "Fast all-optical switching using ion-implanted silicon photonic crystal nanocavities," Appl. Phys. Lett. **90**(3), 031115 (2007).
9. C. Husko, A. De Rossi, S. Combrié, Q. V. Tran, F. Raineri, and C. W. Wong, "Ultrafast all-optical modulation in GaAs photonic crystal cavities," Appl. Phys. Lett. **94**(2), 021111 (2009).
10. K. Nozaki, T. Tanabe, A. Shinya, S. Matsuo, T. Sato, H. Taniyama, and M. Notomi, "Sub-femtojoule all-optical switching using a photonic-crystal nanocavity," Nat. Photonics **4**(7), 477–483 (2010).
11. T. Tanabe, M. Notomi, S. Mitsugi, A. Shinya, and E. Kuramochi, "Fast bistable all-optical switch and memory on a silicon photonic crystal on-chip," Opt. Lett. **30**(19), 2575–2577 (2005).
12. D. M. Beggs, T. P. White, L. O'Faolain, and T. F. Krauss, "Ultracompact and low-power optical switch based on silicon photonic crystals," Opt. Lett. **33**(2), 147–149 (2008).
13. T. Tanabe, H. Taniyama, and M. Notomi, "Carrier diffusion and recombination in photonic crystal nanocavity optical switches," J. Lightwave Technol. **26**(11), 1396–1403 (2008).
14. Y. Halioua, A. Bazin, P. Monnier, T. J. Karle, G. Roelkens, I. Sagnes, R. Raj, and F. Raineri, "Hybrid III-V semiconductor/silicon nanolaser," Opt. Express **19**(10), 9221–9231 (2011).

#199986 - $15.00 USD Received 23 Oct 2013; revised 30 Nov 2013; accepted 2 Dec 2013; published 9 Dec 2013

15. T. Tanabe, K. Nishiguchi, E. Kuramochi, and M. Notomi, "Low power and fast electro-optic silicon modulator with lateral p-i-n embedded photonic crystal nanocavity," Opt. Express **17**(25), 22505–22513 (2009).
16. L. D. Haret, X. Checoury, F. Bayle, N. Cazier, P. Boucaud, S. Combrié, and A. de Rossi, "Schottky MSM junctions for carrier depletion in silicon photonic crystal microcavities," Opt. Express **21**(8), 10324–10334 (2013).
17. C. Manolatou, M. J. Khan, S. H. Fan, P. R. Villeneuve, H. A. Haus, and J. D. Joannopoulos, "Coupling of modes analysis of resonant channel add–drop filters," IEEE J. Quantum Electron. **35**(9), 1322–1331 (1999).
18. Z. Y. Zhang and M. Qiu, "Small-volume waveguide-section high Q microcavities in 2D photonic crystal slabs," Opt. Express **12**(17), 3988–3995 (2004).
19. M. Heuck, S. Combrié, G. Lehoucq, S. Malaguti, G. Bellanca, S. Trillo, P. T. Kristensen, J. Mørk, J. P. Reithmaier, and A. de Rossi, "Heterodyne pump probe measurements of nonlinear dynamics in an indium phosphide photonic crystal cavity," Appl. Phys. Lett. **103**(18), 181120 (2013).
20. Y. Yu, M. Heuck, S. Ek, N. Kuznetsova, K. Yvind, and J. Mørk, "Experimental demonstration of a four-port photonic crystal cross-waveguide structure," Appl. Phys. Lett. **101**(25), 251113 (2012).
21. Q. V. Tran, S. Combrié, P. Colman, and A. De Rossi, "Photonic crystal membrane waveguides with low insertion losses," Appl. Phys. Lett. **95**(6), 061105 (2009).
22. J. D. Joannopoulos, S. G. Johnson, J. N. Winn, and R. D. Meade, *Photonic Crystals, Molding the Flow of Light* (Princeton University, 2008).
23. B. R. Bennett, R. A. Soref, and J. A. Del Alamo, "Carrier-induced change in refractive index of InP, GaAs, and InGaAsP," IEEE J. Quantum Electron. **26**(1), 113–122 (1990).
24. T. J. Johnson, M. Borselli, and O. Painter, "Self-induced optical modulation of the transmission through a high-Q silicon microdisk resonator," Opt. Express **14**(2), 817–831 (2006).
25. P. T. Kristensen, M. Heuck, and J. Mørk, "Optimal switching using coherent control," Appl. Phys. Lett. **102**(4), 041107 (2013).
26. P. E. Barclay, K. Srinivasan, and O. Painter, "Nonlinear response of silicon photonic crystal microresonators excited via an integrated waveguide and fiber taper," Opt. Express **13**(3), 801–820 (2005).
27. X. D. Yang and C. W. Wong, "Coupled-mode theory for stimulated Raman scattering in high-Q/Vm silicon photonic band gap defect cavity lasers," Opt. Express **15**(8), 4763–4780 (2007).
28. P. Lunnemann, S. Ek, K. Yvind, R. Piron, and J. Mørk, "Nonlinear carrier dynamics in a quantum dash optical amplifier," New J. Phys. **14**(1), 013042 (2012).
29. P. T. Kristensen, C. Van Vlack, and S. Hughes, "Generalized effective mode volume for leaky optical cavities," Opt. Lett. **37**(10), 1649–1651 (2012).
30. A. D. Rossi, M. Lauritano, S. Combrié, Q. V. Tran, and C. Husko, "Interplay of plasma-induced and fast thermal nonlinearities in a GaAs-based photonic crystal nanocavity," Phys. Rev. A **79**(4), 043818 (2009).
31. L. D. Haret, T. Tanabe, E. Kuramochi, and M. Notomi, "Extremely low power optical bistability in silicon demonstrated using 1D photonic crystal nanocavity," Opt. Express **17**(23), 21108–21117 (2009).
32. Supplementary information of K. Nozaki, T. Tanabe, A. Shinya, S. Matsuo, T. Sato, H. Taniyama, and M. Notomi, "Sub-femtojoule all-optical switching using a photonic-crystal nanocavity," Nat. Photonics **4**(7), 477–483 (2010).
33. Y. Rosenwaks, Y. Shapira, and D. Huppert, "Picosecond time-resolved luminescence studies of surface and bulk recombination processes in InP," Phys. Rev. B Condens. Matter **45**(16), 9108–9119 (1992).
34. D. Vignaud, J. F. Lampin, and F. Mollot, "Two-photon absorption in InP substrates in the 1.55 μm range," Appl. Phys. Lett. **85**(2), 239–241 (2004).
35. S. Krishnamurthy, Z. G. Yu, L. P. Gonzalez, and S. Guha, "Temperature- and wavelength-dependent two-photon and free-carrier absorption in GaAs, InP, GaInAs, and InAsP," J. Appl. Phys. **109**(3), 033102 (2011).
36. F. G. Della Corte, G. Cocorullo, M. Iodice, and I. Rendina, "Temperature dependence of the thermo-optic coefficient of InP, GaAs, and SiC from room temperature to 600 K at the wavelength of 1.5 μm," Appl. Phys. Lett. **77**(11), 1614–1616 (2000).
37. T. W. Berg, S. Bischoff, I. Magnusdottir, and J. Mørk, "Ultrafast gain recovery and modulation limitations in self-assembled quantum-dot devices," IEEE Photonics Technol. Lett. **13**(6), 541–543 (2001).
38. S. Combrié, G. Lehoucq, S. Malaguti, G. Bellanca, J. P. Reithmaier, S. Trillo, and A. De Rossi, "Two-color switching and wavelength conversion at 10 GHz using a photonic crystal molecule," in *CLEO* (2013), CM4D.5.
39. D. Vukovic, Y. Yu, M. Heuck, S. Ek, N. Kuznetsova, P. Colman, E. Palushani, J. Xu, K. Yvind, L. K. Oxenløwe, J. Mørk, and C. Peucheret, "Wavelength conversion of a 9.35 Gb/s RZ OOK signal in an InP photonic crystal nanocavity," IEEE Photonics Technol. Lett. (to be published).
40. J. Xu, X. L. Zhang, and J. Mørk, "Investigation of patterning effects in ultrafast SOA-based optical switches," IEEE J. Quantum Electron. **46**(1), 87–94 (2010).
41. M. Heuck, P. T. Kristensen, and J. Mørk, "Energy-bandwidth trade-off in all-optical photonic crystal microcavity switches," Opt. Express **19**(19), 18410–18422 (2011).
42. M. Först, J. Niehusmann, T. Plötzing, J. Bolten, T. Wahlbrink, C. Moormann, and H. Kurz, "High-speed all-optical switching in ion-implanted silicon-on-insulator microring resonators," Opt. Lett. **32**(14), 2046–2048 (2007).
43. B. Ellis, M. A. Mayer, G. Shambat, T. Sarmiento, J. Harris, E. E. Haller, and J. Vučković, "Ultralow-threshold electrically pumped quantum-dot photonic-crystal nanocavity laser," Nat. Photonics **5**(5), 297–300 (2011).
44. K. Lengle, M. Gay, A. Bazin, I. Sagnes, R. Braive, P. Monnier, L. Bramerie, N. Nguyen, C. Pareige, R. Madec, J. C. Simon, R. Raj, and F. Raineri, "Fast all-optical 10 Gb/s NRZ wavelength conversion and power limiting function using hybrid InP on SOI nanocavity," in *ECOC* (2012), We.2.E.5.

#199986 - $15.00 USD Received 23 Oct 2013; revised 30 Nov 2013; accepted 2 Dec 2013; published 9 Dec 2013

45. K. Nozaki, A. Shinya, S. Matsuo, T. Sato, E. Kuramochi, and M. Notomi, "Ultralow-energy and high-contrast all-optical switch involving Fano resonance based on coupled photonic crystal nanocavities," Opt. Express **21**(10), 11877–11888 (2013).
46. M. Heuck, P. T. Kristensen, Y. Elesin, and J. Mørk, "Improved switching using Fano resonances in photonic crystal structures," Opt. Lett. **38**(14), 2466–2468 (2013).

1. Introduction

During the past decades, increasing attention has been devoted to developing technologies for optical signal processing and on- and inter-chip optical interconnects [1, 2]. Integrated, ultra-compact and low-energy all-optical switches are promising for increasing the integration density and bandwidth as well as decreasing the energy consumption of future communication networks.

Various kinds of structures have been explored for optical switching such as semiconductor optical amplifiers [3], optical fibers exploiting parametric processes [4], micro-ring cavities [5], photonic crystal (PhC) waveguide Mach-Zehnder interferometers [6], silicon-organic hybrid slot waveguides [7], and photonic crystal cavities [8–10]. Among these, two dimensional PhC membrane structures enabling the realization of waveguides with tailored dispersion as well as nanocavities are promising candidates for high-density integrated photonics. Featuring a high quality factor (Q-factor) and a small mode volume (V), the field intensity can be significantly enhanced inside the cavity (scaling as Q/V) and therefore non-linear signal processing becomes feasible at very low pulse energies [11, 12].

PhC nanocavity switches have been demonstrated experimentally based on carrier effects using different materials. An effective carrier lifetime of about 100 ps was obtained using a silicon structure [8], while a decay time of only 15 ps was realized using a GaAs structure [9]. A PhC switch based on quaternary InGaAsP material, where carriers are generated using a combination of two-photon and linear absorption, showed ultra-low energy operation and a short switching time window of 20 ps with a relaxation process comprising several characteristic time scales [10]. From previous reports, the switching speed is suggested to be limited by the free carrier relaxation process [13]. Though some strategies have been implemented to increase the carrier recovery rate and thereby the switching speed [8, 14–16], few studies have been devoted to investigating the processes governing the dynamics of the switch. Establishing detailed dynamical models is, however, required for further optimization of the performance of the switch, including the investigation of different configurations and applications.

In this article, the dynamics of InP PhC nanocavity structures are investigated experimentally using short-pulse pump-probe measurements. The results are compared with numerical simulations based on coupled mode theory (CMT) [17] and rate equations for the dynamics of the carrier density governing the cavity properties. As a result, we establish an effective numerical model that consistently accounts for the experimental observations.

The paper is structured as follows: In section 2, we describe the design and fabrication of the investigated InP-based PhC nanocavity structures. Then, in section 3, dynamical switching characteristics measured using pump-probe techniques are reported. A dynamical model based on CMT is introduced in section 4 and, in section 5, the different time constants governing the carrier relaxation and their dependence on material parameters are characterized. Section 6 presents fits of the measured dynamics based on the developed model and, in section 7, the model is applied to evaluate the performance of all-optical wavelength conversion. Our conclusions are summarized in section 8.

2. Design and fabrication of a PhC nanocavity structure

As shown in the scanning electron microscope (SEM) images in Figs. 1(a)–1(c), the investigated PhC structure is an InP air-suspended membrane consisting of a defect cavity of the H0 type [18] formed by shifting two neighboring air holes 0.2a in opposite directions, where a is the lattice constant. The cavity is coupled to an input and output waveguide in the Γ-K direction. The waveguides are standard W1 waveguides (defined as the removal of one row of air holes), but with the two innermost arrays of holes shifted towards the waveguide

#199986 - $15.00 USD Received 23 Oct 2013; revised 30 Nov 2013; accepted 2 Dec 2013; published 9 Dec 2013

center by 0.1*a* to make the waveguide fundamental mode overlap in frequency with the cavity mode. Compared with the PhC structures in [9, 19], our structure is realized using a single hole size, which is advantageous from a fabrication point of view.

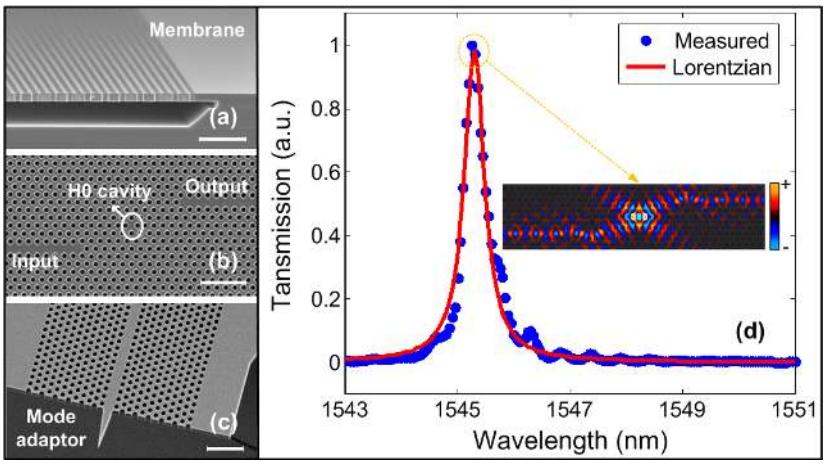

Fig. 1. (a)-(c) SEM images of the fabricated samples. The scale bar corresponds to 2 μm. (d) Linear transmission spectrum of the H0 cavity structure and fit using a Lorentzian function, giving a loaded *Q*-factor of 4100. The inset shows the magnetic field intensity of the resonant mode calculated by FDTD simulations.

The device fabrication process is as follows: The photonic crystal pattern is first defined in positive resist (ZEP520A) by electron-beam lithography and then transferred to a 200 nm Si_3N_4 hard mask by CHF_3/O_2 reactive-ion etching (RIE). The resist is removed and the pattern is transferred to a 340 nm InP layer by a cyclic CH_4/H_2 and O_2 RIE. After removing the Si_3N_4 layer by hydrofluoric acid, the membrane structure is finally formed with diluted H_2SO_4/H_2O_2 to selectively wet-etch a 1 μm $In_{0.53}Ga_{0.47}As$ sacrificial layer located below the membrane [20].

Figure 1(d) plots the measured linear transmission spectrum of one of the fabricated devices for which a = 425 nm, the hole radius is r = 100 nm and the membrane thickness is h = 340 nm. Both the input and output facets of the 800 μm long device are equipped with mode adapters, shown in Fig. 1(c), to facilitate the out coupling [21]. As illustrated in Fig. 1(d), the device has a resonant wavelength at 1545.2 nm. The insertion loss including both coupling and propagation loss is about −17 dB at resonance. The inset in Fig. 1(d) is the calculated magnetic field intensity corresponding to the excitation of the resonant cavity mode, illustrating that the cavity mode couples well to the waveguide mode. The unloaded *Q*-factor estimated using three dimensional finite-difference time-domain (FDTD) simulations is ~2.5×10^4 and the measured loaded *Q*-factor is 4100.

3. Pump-probe setup

A homodyne pump-probe setup, as illustrated in Fig. 2, is used to measure the temporal switching dynamics. The separation of pump and probe beams is accomplished by detuning the signals and selecting the probe using an optical filter. Compared to the heterodyne technique [19], homodyne detection requires spectral separation of pump and probe signals to avoid overlap, but on the other hand allows simple and direct measurement of important properties such as switching contrast and time window.

#199986 - $15.00 USD Received 23 Oct 2013; revised 30 Nov 2013; accepted 2 Dec 2013; published 9 Dec 2013

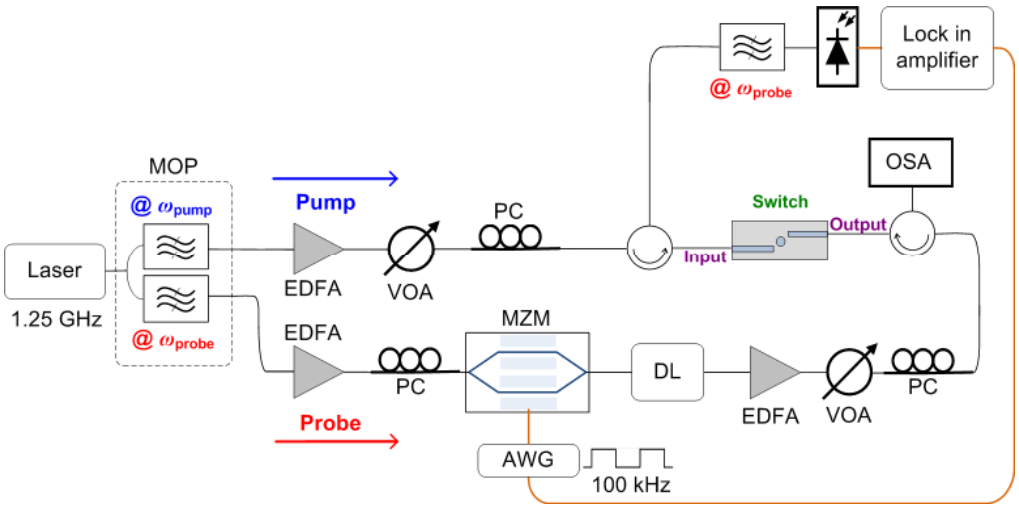

Fig. 2. Experimental setup for measuring the dynamics of the PhC switch. MOP: multiport optical processor; EDFA: erbium doped fiber amplifier; VOA: variable optical attenuator; PC: polarization controller; MZM: Mach-Zehnder modulator; AWG: arbitrary waveform generator; DL: delay line; OSA: optical spectrum analyzer.

A laser source emitting short pulses (full-width at half-maximum, FWHM, of 1.5 ps) at a repetition rate of 1.25 GHz (corresponding to a period longer than the free carrier relaxation time) is employed for the pump-probe measurement. Pump and probe signals are generated by bandpass filtering separate parts of the source spectrum using a multiport optical processor (WaveShaper 4000S). The probe signal is then chopped at 100 kHz using a Mach-Zehnder modulator (MZM) and delayed with respect to the pump using a delay line (DL). A counter-propagating scheme is used to avoid pump-probe interactions in the PhC waveguides. Using polarization controllers, the states of polarization of both pump and probe signals are adjusted to TE polarization [22] and are coupled into and out of the PhC waveguides using lensed single mode fibers. A band-pass filter is used to select the probe signal, while blocking the reflected pump. The transmitted probe signal is then detected with a photodiode, amplified, and monitored with a lock-in amplifier. Pump and probe signals are monitored using power meters and an optical spectrum analyzer, while an infrared camera (Xeva-1.7-320) is mounted on a microscope to image the far-field scattered light from the top of the sample [20]. The probe power is kept sufficiently weak so as not to cause any nonlinear effects in the sample. Typically, the average probe input power is set 7~12 dB lower than the average input pump power and the detuning between the probe and pump is larger than the pump spectral FWHM. For smaller probe power or detuning, interference effects are observed around zero delay.

Figure 3 shows an example of a measured pump-probe signal. The device shows a resonance at 1545.2 nm with a measured loaded Q-factor of 4100 corresponding to a photon lifetime of 3 ps. The switching energy is estimated by subtracting the coupling loss of ~7.5 dB from the pump power at the input fiber. The coupling loss (in dB) is obtained as $(\alpha_{Insertion}-\alpha_{Cavity})/2$ for continuous wave excitation, $\alpha_{Insertion}$ being the device insertion loss and α_{Cavity} the cavity power transmission at resonance, which depends on the ratio between the total and in-plane Q-factor of the cavity. The probe signal is detuned from the cavity resonance to shorter wavelengths by 1 nm (2.6 cavity linewidths), while the center wavelength of the pump is fixed to 1545 nm. The pump and probe pulses are approximately 6 and 12 ps wide, respectively. The inset in Fig. 3 illustrates that the output spectrum of the pump expands towards shorter wavelengths with increasing pump energy, which is consistent with a decrease of the refractive index due to band-filling and free carrier dispersion [23] of carriers excited by two-photon absorption (TPA). From Fig. 3, a switching contrast of 7.8 dB and a FWHM of 18 ps are obtained with a switching energy as low as 85 fJ. This low-energy and fast optical switching is achieved mainly due to the high Q-factor and small mode volume

#199986 - $15.00 USD Received 23 Oct 2013; revised 30 Nov 2013; accepted 2 Dec 2013; published 9 Dec 2013

of the optimized H0 cavity structure. In the following, we analyze the different contributions to the switching dynamics observed in Fig. 3, in particular emphasizing the time constants governing the relaxation process.

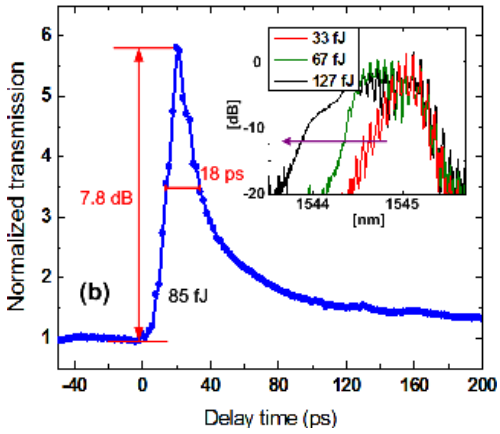

Fig. 3. Measured transmitted probe traces versus time delay between probe and pump pulses. The pump is blocked using an optical filter. The signal is normalized to 1 at large negative delay time, i.e. when the probe transmission is unaffected by the pump. The inset shows output spectra of the pump for different pump energies.

4. Model based on coupled mode theory

To analyze the switching dynamics, we employ coupled mode theory based on an extension of the model presented in [17, 19, 22, 24–27]. The dynamic variables in the model are the field amplitudes inside the cavity, the free-carrier density and the temperature of the membrane. Within first order perturbation theory, the dynamical equations for the cavity modes can be formulated as

$$\dot{a}_p(t) = \left(-\gamma/2 - j(\omega_o + \Delta\omega_p(t) - \omega_p)\right) a_p(t) + \kappa s_p^i(t), \quad (1)$$

$$\dot{a}_s(t) = \left(-\gamma/2 - j(\omega_o + \Delta\omega_s(t) - \omega_s)\right) a_s(t) + \kappa s_s^i(t), \quad (2)$$

$$\Delta\omega_p(t) = -\left(K_{Kerr}\left|a_p(t)\right|^2 - K_{Car}N_c(t) + K_{th}\Delta T(t)\right) - j\left(K_{TPA}\left|a_p(t)\right|^2 + K_{FCA}N_c(t)\right), \quad (3)$$

$$\Delta\omega_s(t) = -\left(2K_{Kerr}\left|a_p(t)\right|^2 - K_{Car}N_c(t) + K_{th}\Delta T(t)\right) - j\left(2K_{TPA}\left|a_p(t)\right|^2 + K_{FCA}N_c(t)\right). \quad (4)$$

Here, $a_{p,s}(t)$ is the amplitude of the slowly varying envelope of the cavity mode excited by the pump and signal (probe), respectively, normalized such that $|a_{p,s}(t)|^2$ represent the corresponding energies in the cavity. The corresponding fields are $A_{p,s}(t) = a_{p,s}(t)\exp(-j\omega_{p,s}t)$, $\omega_{p,s}$ being the center angular frequencies of the input pump and signal, which are represented as $S_{p,s}^i(t) = s_{p,s}^i(t)\exp(-j\omega_{p,s}t)$, with $|s_{p,s}^i|^2$ being the powers of the pump and signal in the input waveguide. Furthermore, ω_o is the cold cavity resonance frequency and $\kappa = \sqrt{\gamma_{in}/2}$ is the coupling coefficient between the cavity and waveguide mode. The total loss rate γ for the cavity has two contributions, $\gamma = \gamma_{in} + \gamma_v$, where γ_{in} accounts for coupling to the waveguides and γ_v represents coupling to all other modes but the relevant waveguide modes, mainly vertical emission. The loss rates can also be related to the cavity in-plane and vertical (unloaded) quality factors, Q_{in} and Q_v, as $\gamma_{in} = \omega_o/Q_{in}$ and $\gamma_v = \omega_o/Q_v$. When the cavity is excited close to its resonance, a highly localized intensity may build up, leading to a change

#199986 - $15.00 USD Received 23 Oct 2013; revised 30 Nov 2013; accepted 2 Dec 2013; published 9 Dec 2013

of the local refractive index due to Kerr effects, free-carrier dispersion (FCD), band filling, as well as thermal effects. The change of the refractive index results in a complex time-dependent change, $\Delta\omega_{p,s}(t)$, of the cavity resonance frequency, as described by Eqs. (3) and (4). The real part of $\Delta\omega_{p,s}(t)$ accounts for the resonance frequency shift while the imaginary part accounts for absorption due to TPA and free-carrier absorption (FCA) [28]. Assuming the signal to be much weaker than the pump, we only account for cavity resonance shifts induced by the pump. Furthermore, we restrict attention to the case of below-bandgap excitation, where carriers are generated by TPA and linear absorption can be neglected. In Eqs. (3) and (4), $K_{Kerr} = \omega_o c n_2 / (n^2 V_{TPA})$ and $K_{TPA} = \beta_{TPA} c^2 / (2n^2 V_{TPA})$ with c being the light speed in vacuum, n the background material refractive index, n_2 its Kerr coefficient, and β_{TPA} the TPA coefficient. The effective TPA mode volume V_{TPA} used to characterize the mode averaged local TPA rate was introduced by Johnson et al. in [24], as integrals of the optical cavity mode. In principle, these integrals diverge because of the leaky nature of the cavity modes [29]. For high-Q cavities, the divergence as a function of integration domain is relatively small, and one can get an estimate of the mode volume by integrating across a finite domain. In the present approach, we use an approximation to the cavity mode obtained from FDTD as the scattered field from the cavity with no waveguides and evaluate the integrals in a volume of about $10 \times 8 \times 1.5$ μm^3. In addition, we neglect the optical confinements [24] because they are found to be almost unity since nearly all the light field is confined in the membrane area. The expansion coefficient K_{Car} has contributions from free-carrier dispersion and band filling, both resulting in a reduction of the refractive index for increasing carrier density. Bandgap shrinkage causes a positive index change, and may be important for small carrier densities, leading to a reduction of K_{Car} [23]. $K_{FCA} = c\sigma / 2n$, where σ is the absorption cross-section for the carrier density $N_c(t)$. Wave mixing (parametric) effects between pump and probe also contribute to the probe field, giving the factor of two difference between Eqs. (3) and (4) for the instantaneous Kerr and TPA effects, while the corresponding effect mediated by carrier density oscillations is neglected, assuming the detuning between the pump and probe to be much larger than the inverse of the carrier lifetime. For thermal dispersion, $K_{th} = \omega_o n_T / n$ in which n_T is the temperature dependence of refractive index. The output signal amplitude of the probe can be obtained as

$$s_s^o(t, \tau_d) = \kappa a_s(t), \tag{5}$$

where τ_d is the time delay of the probe pulse with respect to the pump, as controlled by the delay line. The probe transmission as a function of delay is calculated as the output probe pulse energy normalized by its value at large negative delay

$$T_s(\tau_d) = \frac{\int_{pulse} \left| s_s^o(t, \tau_d) \right|^2 dt}{\int_{pulse} \left| s_s^o(t, -\infty) \right|^2 dt}. \tag{6}$$

The mode averaged temperature difference $\Delta T(t)$ between the PhC cavity and its environment, induced by heating due to the pump pulse, relaxes in several steps [30], but can be approximated by a single decay rate when compared to the faster carrier relaxation

$$\Delta \dot{T}(t) = -\gamma_{th} \Delta T(t) + P_{abs}(t) / C_{InP}. \tag{7}$$

In Eq. (7), $P_{abs}(t) = c\sigma N_c(t) \left| a_p(t) \right|^2 / n + \eta \beta_{TPA} c^2 \left| a_p(t) \right|^4 / (n^2 V_{TPA})$ is the absorbed light power, adding thermal energy to the cavity with the first and second term originating from FCA and TPA, respectively. Notice that only a fraction η of the energy of the two photons involved in

#199986 - $15.00 USD Received 23 Oct 2013; revised 30 Nov 2013; accepted 2 Dec 2013; published 9 Dec 2013

the TPA process is converted into thermal energy (kinetic energy of the electrons). The remaining part is used to overcome the semiconductor bandgap energy E_g. We estimate $\eta = (2\hbar\omega_p - E_g)/2\hbar\omega_p \approx 17\%$. C_{InP} is the thermal capacitance of the PhC membrane structure which is a product of material density, heat capacity and cavity volume [27]. γ_{th} is the thermal relaxation rate, which can be estimated using a finite-element method (FEM) [30, 31].

5. Carrier dynamics

5.1 Carrier diffusion simulations

The carrier dynamics in the PhC cavity is first investigated through FEM simulations. We consider an effective two-dimensional system, where the dynamics on the small length scale corresponding to the membrane thickness is neglected by the consideration of an effective carrier lifetime. This approach was shown to account for experimental results [13, 32]. The spatial and temporal variation of the carrier density $N(x,y,t)$ is governed by the following equation:

$$\dot{N}(x,y,t) = D_a \nabla^2 N(x,y,t) - N(x,y,t)/\tau_e. \tag{8}$$

In Eq. (8), $\tau_e = (1/\tau_b + 2S/h)^{-1}$ is the effective carrier lifetime, with contributions due to bulk recombination, with lifetime τ_b, and surface recombination, S being the PhC surface recombination velocity and h the PhC membrane thickness. D_a is the material ambipolar diffusion coefficient. Normally, if the imbalances between the electron and hole densities as well as their fluxes are small, the ambipolar approximation can well describe the carrier transportations. At the PhC surface, Neumann boundary conditions are applied $D_a \nabla N(x,y,t) = -SN(x,y,t)$.

Equation (8) is solved subject to an initial carrier distribution, generated by the pump pulse via TPA, which is taken to be proportional to the square of the light intensity with a distribution following the cavity field profile $\varepsilon(x,y)|E(x,y)|^4$. For use in CMT, we do not need the full spatial variation of the carrier density, but rather a mode averaged carrier density, $N_c(t)$, which can be expressed as

$$N_c(t) = \frac{\iint N(x,y,t)\varepsilon(x,y)\left|E(x,y)\right|^2 dxdy}{\iint \varepsilon(x,y)\left|E(x,y)\right|^2 dxdy}. \tag{9}$$

In the simulations, we use the same parameters as in the experiments, i.e. the investigated structure is a PhC H0 cavity as the fabricated one with a = 425 nm, r = 100 nm, h = 340 nm and the cavity hole shift is 0.2a. We use D_a = 10 cm^2/s for InP corresponding to a mobility of 5400 cm^2/(V·s) for the electrons and 200 cm^2/(V·s) for the holes.

Figure 4 shows the calculated temporal variations of the effective carrier density for different parameter values. It is observed that the relaxation process contains both fast and slow components. Figure 4(a) illustrates the dependence of the carrier density on its initial spatial profile. The red curve corresponds to an initial profile $\propto \varepsilon(x,y)|E(x,y)|^4$, while the others correspond to a profile determined by the overlap of two identical Gaussian distributions with FWHM values of R_I and their maxima placed at the two primary antinodes of the cavity field $\varepsilon(x,y)|E(x,y)|^4$. From Fig. 4(a), where surface and carrier bulk recombination are not included, we find that the initial cavity mode distribution affects only the fast carrier decay rate but not the slow one, for which the carrier spatial distribution has become uniform, as seen in the insets of Fig. 4(a). Figure 4(b) illustrates the dependence on the ambipolar diffusion coefficient D_a, when the initial carrier profile is fixed ($\propto \varepsilon(x,y)|E(x,y)|^4$), and the surface and bulk carrier decay rates are set to zero. It is found that D_a affects both the fast and slow carrier relaxation rates. Figure 4(c) shows the result of varying the surface recombination rate S. The initial carrier profile is again fixed ($\propto \varepsilon(x,y)|E(x,y)|^4$), D_a = 10 cm^2/s

#199986 - $15.00 USD Received 23 Oct 2013; revised 30 Nov 2013; accepted 2 Dec 2013; published 9 Dec 2013

and the bulk carrier decay rate is set to zero. It is seen that surface recombination affects the slow carrier relaxation tail significantly but has negligible influence on the fast relaxation. Figure 4(d) illustrates the dependence of the dynamics on the bulk carrier recombination rate for fixed surface recombination rate $S = 2 \times 10^4$ cm/s. For InP, τ_b has a typical value spanning from tens to several hundreds of nanoseconds [33]. As τ_b decreases, the slow relaxation rate increases slightly while the fast relaxation rate remains almost the same. These results show that the carrier relaxation dynamics is mainly determined by carrier diffusion and surface recombination.

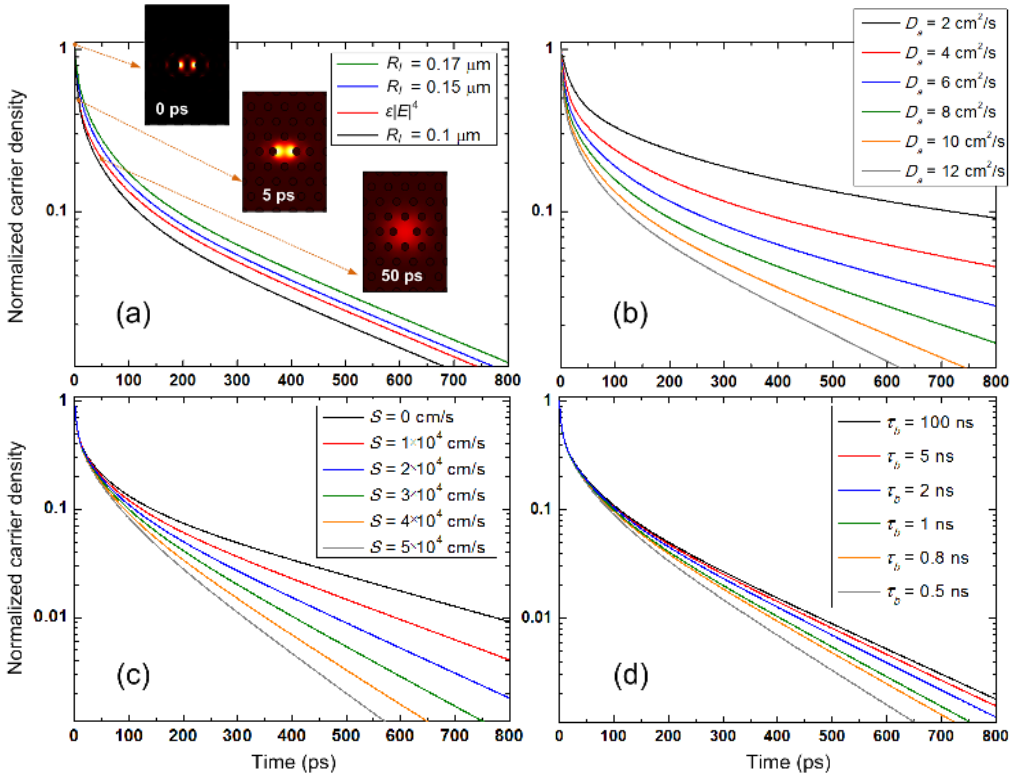

Fig. 4. Calculated effective carrier density versus time for different (a) initial carrier density profiles (S = 0 cm/s, $\tau_b = \infty$); (b) diffusion coefficients (S = 0 cm/s, $\tau_b = \infty$); (c) surface recombination velocities ($\tau_b = \infty$); (d) carrier bulk lifetimes ($S = 2 \times 10^4$ cm/s). The insets in (a) show the profiles of the carrier density distribution at 0 ps, 5 ps and 50 ps, respectively. The carrier densities are normalized to 1 at $t = 0$.

5.2 Carrier rate equations

Based on the FEM simulation results, we formulate a phenomenological rate equation model for the carrier dynamics that can readily be combined with the CMT for the optical fields to describe the switching dynamics. Unlike most previous work [24–27, 30], which employ only one carrier rate equation with a single decay rate, we find it necessary to use three coupled carrier rate equations containing three characteristic time constants to accurately describe the carrier dynamics:

$$\dot{N}_c(t) = -\left(N_c(t) - N_2(t)\right)/\tau_1 - N_c(t)/\tau_3 + G(t), \tag{10}$$

$$\dot{N}_2(t) = -\left(N_2(t) - N_3(t)\right)/\tau_2 + \left(N_c(t) - N_2(t)\right)/\tau_1 \times R_{12} - N_2(t)/\tau_3, \tag{11}$$

$$\dot{N}_3(t) = \left(N_2(t) - N_3(t)\right)/\tau_2 \times R_{23} - N_3(t)/\tau_3, \tag{12}$$

#199986 - $15.00 USD Received 23 Oct 2013; revised 30 Nov 2013; accepted 2 Dec 2013; published 9 Dec 2013

$N_c(t)$ is the effective carrier density in the region defined by the cavity resonant mode profile, cf. Eq. (9). The carrier density $N_c(t)$ couples with a short time constant τ_1 to a density N_2(t) defined as the density in a larger neighboring area, thus mainly accounting for the initial fast decay of $N_c(t)$ due to fast diffusion. The density N_2(t) subsequently couples with time constant τ_2 to N_3(t), being the density in a yet larger neighboring region as in the insets of Fig. 4(a). The need to introduce several carrier densities arises due to the non-exponential relaxation implied by the diffusion process. In addition, all the carrier populations are subject to bulk and surface recombination with a time constant τ_3. As we shall see later, τ_3 may actually also have a small contribution from (slow) carrier diffusion, when the total recombination rate is small. In Eqs. (11) and (12), R_{12} and R_{23} represent the ratios between the carrier volume of $N_c(t)$ and N_2(t), and between the carrier volume of $N_2(t)$ and N_3(t), respectively, and reflect the conservation of carriers when they are exchanged between the different volumes. Furthermore, $G(t) = \beta_{TPA} c^2 \left|a_p(t)\right|^4 / (2\hbar\omega_p n^2 V_{FCA}^2)$ is the carrier generation term due to TPA, with the effective FCA mode volume V_{FCA} characterizing the mode averaged free carrier density generated by TPA [24].

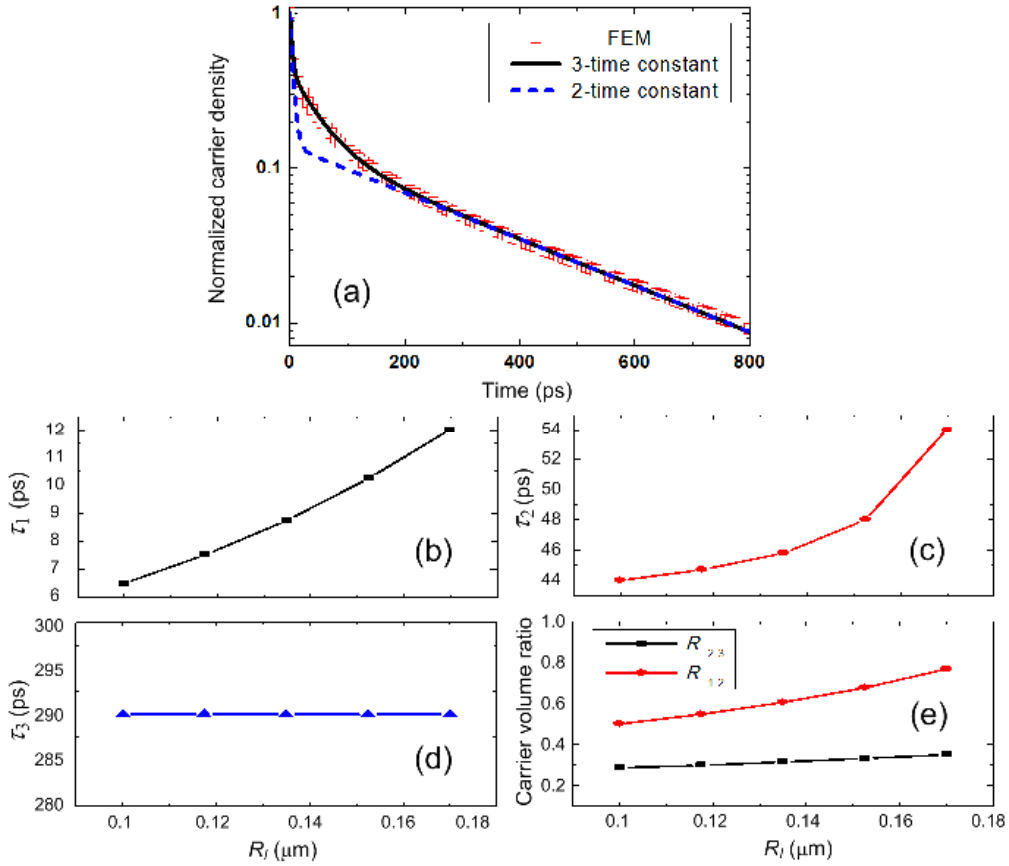

Fig. 5. (a) Effective carrier density versus time calculated using FEM, 3-time constant rate equations and 2-time constant rate equations (S = 0 cm/s, $\tau_b = \infty$). Dependence of (b) τ_1, (c) τ_2, (d) τ_3, (e) R_{12} and R_{23} on the initial carrier density profile (S = 0 cm/s, $1/\tau_b$ = 0). All the plots correspond to D_a = 10 cm^2/s.

In order to investigate the validity of the 3-time constant model, Fig. 5(a) compares the calculated results using FEM and 3-time constant rate equations with optimized fitting parameters. The generation term $G(t)$ in Eq. (10) is set to be zero, the initial carrier profile is given by $\varepsilon(x,y)|E(x,y)|^4$ and we consider S = 0 cm/s and $1/\tau_b$ = 0. For comparison, a simulation

#199986 - $15.00 USD Received 23 Oct 2013; revised 30 Nov 2013; accepted 2 Dec 2013; published 9 Dec 2013

result using 2-time constant rate equations as in [19] is also plotted with optimized fitting parameters. Figure 5(a) suggests that the relaxation curves can be fitted well using the 3-time constant model, while the 2-time constant model introduces an obvious kink between the fast and slow decay components.

By fitting the FEM solutions with the 3-time constant model, we obtain the dependence of the time constants τ_1, τ_2, τ_3 and the carrier volume ratios R_{12}, R_{23} on the initial carrier density profile, cf. Figs. 5(b)–5(e). The initial profile is again set as the overlap of two identical Gaussian distributions with a FWHM R_I. Carrier band-to-band recombination is not considered. As R_I increases, meaning the initial profile expands, R_{12} and R_{23} increase as illustrated in Fig. 5(e). From Figs. 5(b)–5(d), the fast time constant τ_1 (several picoseconds) and τ_2 (several tens of picoseconds) increase with R_I while the slow time constant τ_3 (several hundreds of picoseconds) remains almost the same. This is as expected, since a more localized carrier profile gives faster initial carrier diffusion, while the following slow diffusion is not mode dependent since the broadened carrier distribution behaves similarly to that of a cavity-free PhC, only being affected by the effective diffusion coefficient determined by the material and structure of the PhC.

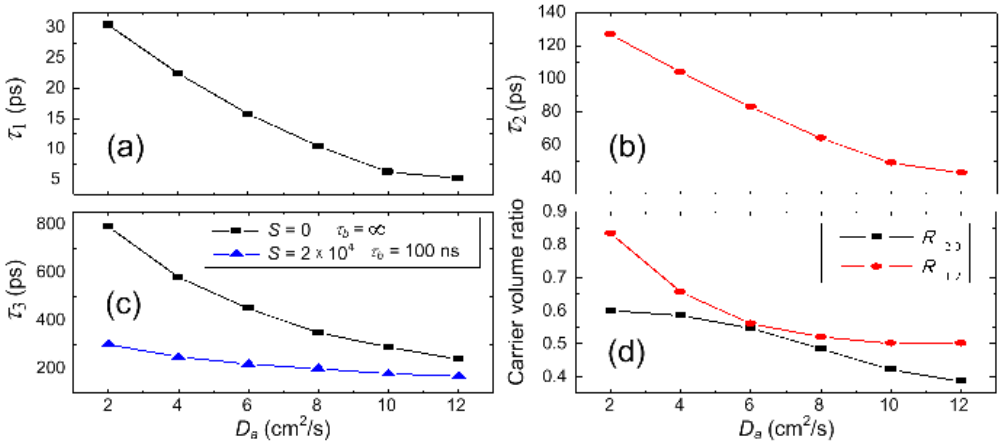

Fig. 6. Dependence of the time constants and carrier volume ratios in the rate equation model on the carrier diffusion coefficient. Variation of (a) τ_1, (b) τ_2, (c) τ_3, and (d) R_{12} and R_{23}. The initial carrier density profile is proportional to $\varepsilon(x,y)|E(x,y)|^4$, and $S = 0$ cm/s, $1/\tau_b = 0$.

Figure 6(a) shows the dependence of the time constants τ_1, τ_2, τ_3 and the carrier volume ratios R_{12}, R_{23} on the carrier diffusion coefficient. The initial carrier profile was set proportional to $\varepsilon(x,y)|E(x,y)|^4$, $S = 0$ cm/s and $1/\tau_b = 0$. As expected, all time constants decrease when the carrier diffusion coefficient increases. From Fig. 6(c), when the recombination rate is finite, for example, $S = 2 \times 10^4$ cm/s and $\tau_b = 100$ ns, which are typical values for InP PhC membrane structures, we find that τ_3 only depends weakly on D_a, implying that it is mainly determined by surface and carrier bulk recombination, which is also the implicit assumption about the form used for the rate equation, which corresponds to the total carrier number decaying with a time constant τ_3.

Figure 7(a) shows the variation of the time constants τ_1, τ_2, τ_3 with the surface recombination velocity S for $1/\tau_b = 0$. While τ_1 and τ_2 do not vary with S, τ_3 decreases significantly from an upper value (the longest time constant) of 290 ps originating from slow carrier diffusion. The tendency is similar when varying the bulk recombination rate $1/\tau_b$, cf. Fig. 7(b). The short relaxation times are nearly constant while the slowest vary, albeit much less compared to the dependence on the surface recombination velocity. From the fitting to FEM simulations, we find that the carrier volume ratios depend weakly on S and τ_b and remain approximately constant at $R_{12} = 0.5$ and $R_{23} = 0.4$. This means that, like the fast time constants τ_1 and τ_2, the carrier volumes depend only on the initial carrier profile and the effective diffusion coefficient of the structure. While the modeling of the carrier density

#199986 - $15.00 USD Received 23 Oct 2013; revised 30 Nov 2013; accepted 2 Dec 2013; published 9 Dec 2013

dynamics in terms of three carrier densities is an approximate representation of the diffusion and recombination processes in the PhC membrane, the dependence of model parameters on material constants and excitation conditions supports the interpretation of the different carrier densities.

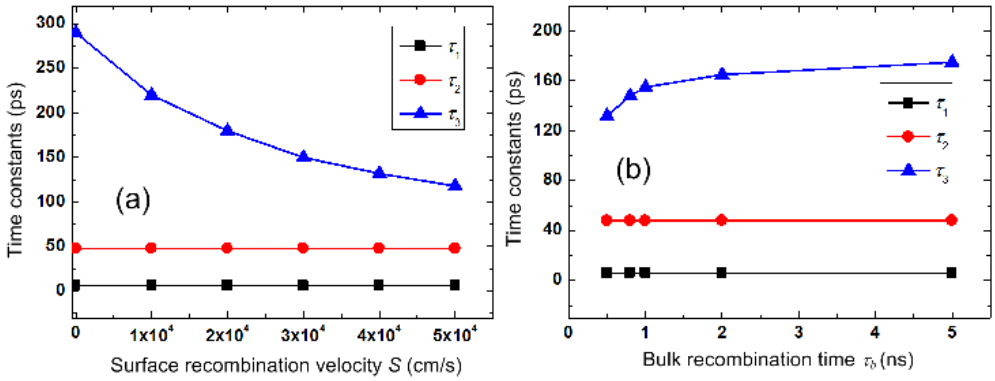

Fig. 7. (a) Dependence of the time constants τ_1, τ_2, τ_3 on the surface recombination velocity S ($1/\tau_b = 0$). (b) Dependence of the time constants τ_1, τ_2, τ_3 on the carrier bulk lifetime τ_b ($S = 2 \times 10^4$ cm/s).

6. Comparison between experiment and theory

The CMT model including the dynamics of the cavity field, carrier density and membrane temperature has now been formulated and will be compared to the pump-probe measurements.

Table 1. Parameters Used for CMT Calculations

Symbol	Value	Source	Symbol	Value	Source
V_{TPA}	0.21 μm^3	FDTD	γ_{th}	1.6×10^8 s^{-1}	FEM
V_{FCA}	0.13 μm^3	FDTD	n_T	2.01×10^{-4} K^{-1}	[36]
β_{TPA}	24 cm/GW	[34]	n	3.17	[20]
n_2	16.5×10^{-18} m^2/W	Fit	K_{Car}	1.95×10^{-12} m^3/s	Fit
σ	4.5×10^{-21} m^2	[35]	Q	4100, 1200	Measured
C_{InP}	3.6×10^{-13} s.W/K	FEM	Q_v	25000	FDTD

Using the physical parameters shown in Table 1, simulations are carried out by solving Eqs. (1)–(7) and Eqs. (10)–(12) numerically, which is readily accomplished using a standard routine for solving ordinary differential equations.

Figure 8 shows the measured (dots) and simulated (lines) probe transmission versus pump-probe delay for different pump energies and two different probe detunings δ, corresponding to switch-on and switch-off configurations. The corresponding spectral configurations of pump, probe and cavity are also illustrated. Two different samples are considered, Figs. 8(a) and 8(b), with similar H0 cavity structures but different Q-factors. In all cases we find excellent agreement between measurements and simulations using the CMT model employing three carrier rate equations. In all cases the transmission recovers in two steps, a fast and a slow one, confirming previous findings [9]. We emphasize, however, that it was not possible to obtain quantitative agreement employing a model considering only two carrier densities and two time constants.

#199986 - $15.00 USD Received 23 Oct 2013; revised 30 Nov 2013; accepted 2 Dec 2013; published 9 Dec 2013

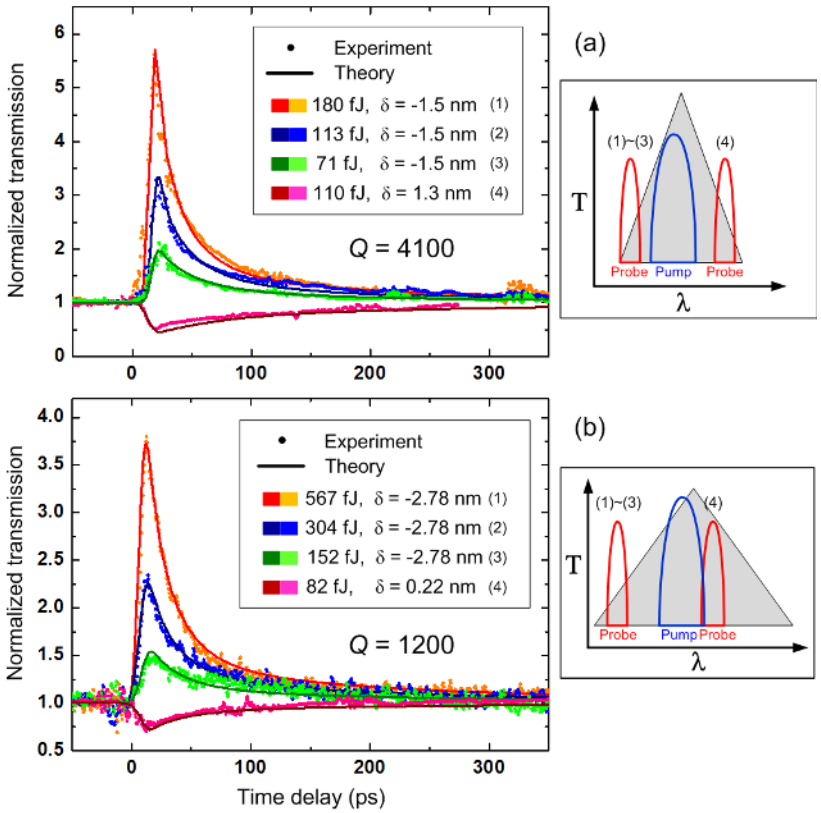

Fig. 8. Left: measured (markers) and simulated (solid lines) probe transmission versus delay between pump and probe pulses for different pump energies and probe detunings. The transmission is normalized to 1 when the probe precedes the pump. The probe pulse width is ~9 ps, and the pump pulse width is 5-6 ps. Right: schematic illustration of the spectral locations of probe (red), pump (blue) and cavity spectrum (grey shaded). (a) The cavity resonance is at 1545.2 nm and the *Q*-factor is 4100. The pump wavelength is fixed at 1545 nm and two different probe locations are considered. (b) The cavity resonance is at 1541.78 nm and the *Q*-factor is 1200. The pump wavelength is fixed at 1541.5 nm and two different probe locations are considered.

In Fig. 8(a), all the traces correspond to a fixed set of carrier time constants and carrier volume ratios: $\tau_1 = 3$ ps, $\tau_2 = 85$ ps, $\tau_3 = 180$ ps, $R_{12} = 0.5$, $R_{23} = 0.4$. For Fig. 8(b) we similarly have: $\tau_1 = 3$ ps, $\tau_2 = 45$ ps, $\tau_3 = 175$ ps, $R_{12} = 0.5$, $R_{23} = 0.3$. The measurement data from the two structures were fitted independently: The fact that similar values are obtained suggests that these are related to intrinsic structural properties, supporting the appropriateness of the phenomenological model formulated in Section 5. From the comparison between simulations and experiments, it can be concluded that thermal effects are negligible at this low signal repetition rate (the calculated thermal induced resonance red shift is less than 0.02 nm) due to the high thermal conductivity of InP.

For the switch-on case ($\delta < 0$), the switching contrast increases with the pump energy. When the strong pump pulse is injected into the cavity, the probe transmission is first reduced due to the combination of TPA loss and the instantaneous Kerr effect, which red shifts the resonance. However, this reduction is relatively small and therefore not noticeable in the experiments unless very large pump powers are used. Following the Kerr effect, free carriers are generated by TPA, causing strong carrier-induced nonlinearity which dominates over the thermo-optic effect, shifting the cavity resonance towards shorter wavelengths, hence increasing the probe transmission. For the switch-off case ($\delta > 0$), in contrast, the blue-shift of the cavity resonance causes a reduction of the probe transmission. Comparing the results in

#199986 - $15.00 USD Received 23 Oct 2013; revised 30 Nov 2013; accepted 2 Dec 2013; published 9 Dec 2013

Figs. 8(a) and 8(b), shows that the switching contrast is larger, the switching energy is smaller and the switching window is shorter for the structure with higher *Q*-factor mainly due to the sharper slope of the resonant line. A very high *Q*-factor can, however, limit the signal operation speed and make it difficult to avoid cross-talk between pump and probe. In Fig. 8(a), a switching contrast of nearly 8 dB can be achieved for switch-on with an energy of 180 fJ. According to the simulations, the absorbed energy due to TPA and FCA is of the order of 20 fJ.

7. Patterning effects in all-optical wavelength conversion

While a major part of the transmission induced by the pump recovers within tens of picoseconds, it is well-known that a slow component, albeit small, may lead to detrimental patterning effects [37]. Thus, after verifying our CMT model, we apply it, as an example, to evaluate the role of the carrier dynamics on the performance of the nanocavity for all-optical wavelength conversion [38, 39].

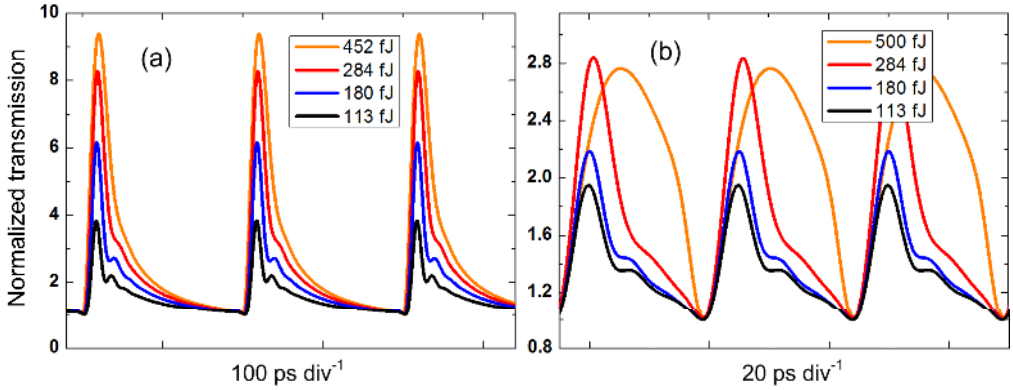

Fig. 9. Simulation of wavelength conversion using a PhC switch. The probe signal intensity is shown versus time for a pump signal at repetition rates of (a) 10 GHz and (b) 40 GHz for different pump energies. The pump signal has a center wavelength of 1545 nm. The input probe is a weak continuous wave signal with a detuning of −1.5 nm from the cavity resonance of 1545.2 nm. The other parameters are the same as in Fig. 8(a).

Figure 9 shows the calculated probe transmission in the switch-on case when the pump consists of 5 ps FWHM Gaussian pulses at 10 GHz and 40 GHz repetition rates, respectively. The injected pump signal corresponds to a sequence of consecutive "1's", the input probe is a weak continuous wave signal with a detuning of −1.5 nm from the cavity resonance of 1545.2 nm. The simulation results are obtained when the output signals reach steady states. Instead of using pseudorandom binary sequences, patterning effects can also be tested using a periodic signal by investigating the dependence of the extinction ratio on the period [40]. Figure 9(a) shows that, at a repetition rate of 10 GHz, the switch fully recovers to the initial state in-between pump pulses and a large modulation depth can be achieved with a high pump energy. However, at a higher repetition rate of 40 GHz, as shown in Fig. 9(b), the extinction ratio degrades, i.e. patterning effects become serious and the switching performance is deteriorated. In this case, there is a maximum in the modulation depth as a function of pump energy. This fact can be attributed to three factors. First, for very large energies, the cavity resonance has already shifted far away from the pump spectrum due to a large density of accumulated free carriers caused by the slow carrier relaxation. Then, injecting a stronger pump, will not increase the resonance shift, since only the initial part of the pump is coupled to the cavity. Second, at large pump powers, the cavity transmission maximum may shift across the probe wavelength leading to a decrease of the probe transmission. Finally, a larger density of free carriers will cause larger FCA, thus reducing the probe transmission.

In Fig. 9, a transient oscillation of the probe transmission curve is seen, which can be explained as resulting from interference between the probe signal and the cavity mode [41].

#199986 - $15.00 USD Received 23 Oct 2013; revised 30 Nov 2013; accepted 2 Dec 2013; published 9 Dec 2013

When the switching energy is low, the frequency difference between the cavity mode and probe is large, so the beating period is short and the oscillations can be clearly seen. However, as the pump energy increases, the cavity resonance blue shifts closer to the probe and the beating period becomes longer and the oscillations are no longer visible due to the overall transmission decay. These beating-induced oscillations can introduce a decay of energy faster than the cavity photon lifetime and it was recently suggested to use such coherent effects to improve the performance of the switch [25].

From the results in Fig. 9, it can be concluded that the wavelength conversion performance, especially at high repetition rates, is seriously affected by the slow carrier recovery process. To improve the performance, the time constants can be decreased by implementing strategies such as capturing carriers by impurities [8, 42] or quantum wells [14], employing a thinner membrane, sweeping out carriers using electric contacts [16, 43], or doping with n-type carriers to reduce the ambipolar lifetime. The Q-factor should be chosen so that the dynamics is not limited by the cavity photon lifetime [41]. Also, other PhC structures may be employed to improve the switching performance, such as multi-mode and multi-port cavity structures employing a low-Q mode for the probe [20, 38, 44], and Fano structures [45, 46]. Although the switching speed is one of the most important characteristics of the switch, it should be noted that simply increasing the carrier relaxation rate will increase the energy consumption, since it will reduce the accumulation of carriers during the pump excitation, which will affect the switching contrast as well. This energy-bandwidth trade-off [41] is a major issue for nonlinear optical switches and needs to be further investigated in systems experiments.

8. Conclusion

The carrier dynamics and switching characteristics of an InP photonic crystal H0 nanocavity were experimentally investigated using pump-probe measurements. The results were compared to simulations using a model based on coupled-mode theory and a rate equation description of the carrier dynamics. Excellent agreement between measurements and simulations was obtained when employing a model containing three relaxation times, accounting for the joint effects of carrier diffusion, surface recombination and bulk recombination. The dependence of the parameters entering the rate equation model on the physical material parameters for the switch was deduced by numerical simulations of the diffusion equation, confirming the relevance of the suggested rate equation model and its physical interpretation. The model was next applied to analyze the role of the fast and slow carrier relaxation processes on patterning effects in the device, as exemplified by the case of all-optical wavelength conversion. It was shown that although a short switching window may be realized by exploiting fast carrier diffusion effects, the accumulation of carriers due to slow (bulk and surface) recombination in the cavity region may be detrimental at high repetition rates. Further investigations of these limitations and alternative structures for alleviating them are thus needed. The coupled-mode theory model suggested in this paper can be used to analyze various applications and structures, and furthermore has a form that can be easily extended to include additional effects, thus making it useful for exploring the potential of nanocavity switches for systems applications.

Acknowledgments

The authors acknowledge financial support from Villum Fonden, via the NATEC (NAnophotonics for TErabit Communications) Centre, and the European Union (COPERNICUS project, FP-ICP-249012).